

IMA Journal of Applied Mathematics (2007) 1–26
 doi:10.1093/imamat/hxm046

A combined BIE-FE method for the Stokes equations

A. V. LUKYANOV[†]

Department of Mathematics, University of Reading, Reading RG6 6AX, UK

AND

Y. D. SHIKHMURZAEV AND A. C. KING

School of Mathematics, University of Birmingham, Birmingham B15 2TT, UK

[Received on 1 December 2006; accepted on 14 March 2007]

A numerical algorithm for the biharmonic equation in domains with piecewise smooth boundaries is presented. It is intended for problems describing the Stokes flow in the situations where one has corners or cusps formed by parts of the domain boundary and, due to the nature of the boundary conditions on these parts of the boundary, these regions have a global effect on the shape of the whole domain and hence have to be resolved with sufficient accuracy. The algorithm combines the boundary integral equation method for the main part of the flow domain and the finite-element method which is used to resolve the corner/cusp regions. Two parts of the solution are matched along a numerical ‘internal interface’ or, as a variant, two interfaces, and they are determined simultaneously by inverting a combined matrix in the course of iterations. The algorithm is illustrated by considering the flow configuration of ‘curtain coating’, a flow where a sheet of liquid impinges onto a moving solid substrate, which is particularly sensitive to what happens in the corner region formed, physically, by the free surface and the solid boundary. The ‘moving contact line problem’ is addressed in the framework of an earlier developed interface formation model which treats the dynamic contact angle as part of the solution, as opposed to it being a prescribed function of the contact line speed, as in the so-called ‘slip models’.

Keywords: Dynamic contact angle; finite elements; free surface flows; hybrid numerical technique; Stokes equations.

1. Introduction

The necessity to describe low Reynolds number free surface flows arises in many modern applications of fluid mechanics, especially in microfluidics and biological processes, where the volumes involved are often on the nanoliter scale (Squires & Quake, 2005) and, even for low-viscosity fluids, like water, the Reynolds numbers characterizing the flow can be of the order of 10^{-6} . The complexity of the mathematical problems one encounters in the applications calls for efficient and flexible numerical algorithms capable of handling a wide range flow conditions and geometries.

A powerful numerical algorithm of solving free boundary problems intensively used in the past two decades is the finite-element method (FEM) based on tessellating the flow domain into finite elements and using the Galerkin approximation of the bulk equations on each of them (Gresho & Sani, 2000). However, the straightforwardness of this approach becomes its disadvantage in the situations where the geometry of the flow domain is complex so that tessellation turns into a non-trivial problem and remeshing the grid in the process of iterations causes additional difficulties of controlling the

[†]Email: a.lukyanov@reading.ac.uk

computational accuracy. This disadvantage is particularly obvious in the case of the Stokes flows where an exact analytic free space solution to the bulk equations is available (Pozrikidis, 1992).

The exact solution to the Stokes equations is utilized in the boundary integral equation method (BIEM) where the problem is reduced to that on the boundaries confining the flow domain. This allows one to reduce the dimensionality of the problem and eliminate the difficulties caused by the complex geometry of the domain. The method has been used to describe a wide variety of flows (Jaswon *et al.*, 1967; Jaswon & Symm, 1977; Rallison & Acrivos, 1978; Kelmanson, 1983a,b, 2004; Pozrikidis, 1992; Zinchenko *et al.*, 1999; Zinchenko & Davis, 2002). The problem arises when the boundary of the flow domain has sharp corners or cusps (Jaswon *et al.*, 1967; Jaswon & Symm, 1977; Kelmanson, 1983b, 2004; Pozrikidis, 1992; Zinchenko *et al.*, 1999). Computations show that for non-trivial flows near a corner, the numerical solution oscillates (Jaswon *et al.*, 1967; Jaswon & Symm, 1977) thus making it impossible to achieve the required accuracy. The situation becomes even less satisfactory in an often encountered situation where the flow variables have large gradients near the corner. In this case, the combined effect of all adverse factors leads to poor conditioned matrices and the loss of accuracy and convergence (Kelmanson, 1983b, 2004; Zinchenko *et al.*, 1999).

In the case of corners formed by solid boundaries, a way of dealing with large gradients of the flow variables has been proposed by Kelmanson (1983b), who factored out the singular part of the solution to improve conditioning and convergence. Naturally, this method requires an *a priori* knowledge of the shape of the corner and of the asymptotic form of the singularity. A largely similar approach has been used by Zinchenko *et al.* (1999) to develop a curvatureless algorithm for flows near regions of the free boundary, where the free surface curvature can become singular as the flow evolves. This method of taking out the singularity (which in itself could be an artifact from the physical viewpoint) allows one to substantially improve convergence of the algorithm though the problem as such remains (Kelmanson, 2004).

The aforementioned problem turns into a difficulty of principle in the situation where the flow parameters near the corner have a global effect on the flow domain and hence poor accuracy has catastrophic consequences. Most notably, this is the case in the modelling of dynamic wetting where, on the one hand, the boundary of the flow domain is invariably non-smooth as it has the ‘contact angle’ formed by the free surface and the solid boundary at the ‘contact line’ and, on the other, as experiments show (Blake *et al.*, 1999) and hence the mathematical model must follow, the value of the contact angle depends on the flow field near the contact line. Then, even relatively small computational errors, and especially oscillations of the solution near the contact line, will result in errors in the contact angle which, being the boundary condition for the equation determining the free surface shape, will generate global errors and spurious large-amplitude waves on the free surface and in the bulk. The latter will come back to the contact line region causing more (this time, induced) oscillations in the flow parameters.

In the present paper, we develop a combined BIE-FE method that uses advantages and, to a large extent, compensates disadvantages of the two constituent techniques. The idea is as follows. One can single out a region with a relatively simple geometry to include the singularity of curvature of the flow domain’s boundary (a corner or an inward-pointing cusp (An outward-pointing cusp and a contact angle equal to 0° are a special case and require some analytic work before they can be incorporated into a numerical code.)) and use there the full power of the FEM to compute the flow parameters with very high accuracy and spatial resolution. Outside this region, the standard BIEM can be used to efficiently handle the overall Stokes flow. The two regions are separated by an artificial ‘internal interface’ where the flow variables expressed in terms of the two methods must be matched with sufficient smoothness. The range of positions and shapes of the internal interface must be chosen in such a way that, on the one hand, this interface is sufficiently close to the corner to ensure simplicity of the domain subject

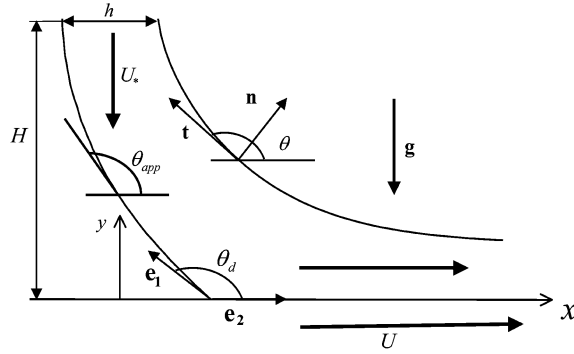


FIG. 1. Definition sketch for curtain coating. θ_d is the ‘actual’ contact angle, i.e. the angle at which the free surface meets a solid boundary in the macroscopic fluid mechanics modelling of the flow, i.e. the angle used as a boundary condition for the equation determining the shape of the free surface; θ_{app} is the so-called ‘apparent’ contact angle often used as an adjustable parameter in interpreting the results of experiments.

to the FEM and avoid tessellation of large spaces and, on the other hand, it must be sufficiently far away from the corner to avoid having a high curvature and hence compromising the accuracy of the BIEM. Besides this, the shape of the internal interface has to make the boundary of the BIEM domain sufficiently smooth and at the same time it should not degenerate the finite elements adjacent to the points where the internal interface and the actual boundaries of the flow domain intersect. Naturally, there should be no variation of the computed flow parameters caused by shifting the internal interface that would be outside the overall accuracy of the method.

The idea of splitting the computational domain into exterior and interior parts where different methods operate is not new and has been previously utilized in hybrid techniques to solve problems involving a combination of components with essentially different physical properties (Marquez *et al.*, 2004; Li & Aluru, 2004; Ballandras *et al.*, 2004). For example, Marquez *et al.* (2004) used a hybrid technique to simulate fluid–solid interactions in acoustic problems. The solid vibrations and the near-field effects have been approximated by means of the FEM, whereas the far-field dynamics for an inviscid liquid has been solved using the BIEM. In a slightly different way, a hybrid algorithm has been utilized to carry out electrostatic analysis of nanoelectromechanical systems (Li & Aluru, 2004) and to simulate surface acoustic wave devices built on stratified media (Ballandras *et al.*, 2004). Obviously, a necessary condition to use a hybrid technique of that kind is the availability of an analytic solution in the exterior domain to apply the BIEM, e.g. a solution to the Laplace equation (Marquez *et al.*, 2004). In our combined method, the exterior problem is set up for the Stokes equations with the classical set of boundary conditions.

We will illustrate the new algorithm by considering the flow known as ‘curtain coating’. Curtain coating, where a sheet of liquid impinges onto a moving solid substrate (Fig. 1), is used in applications as an efficient way of depositing thin liquid films on solid surfaces (Kistler & Schweizer, 1997). As a basis for the numerical code, we will use the theory of dynamic wetting as an interface formation process (Shikhmurzaev, 1993, 1994, 2006, 2007), which, to date, is the only model where the dynamic contact angle is part of the solution rather than an input.

2. The problem formulation

We will be looking for a solution of the Stokes equations

$$\nabla \cdot \mathbf{u} = 0, \quad \nabla p = \mu \nabla^2 \mathbf{u} + \rho \mathbf{g} \quad (1)$$

in the flow configuration shown in Fig. 1 subject to the following boundary conditions. On an unknown free surface with the outward normal \mathbf{n} , the boundary conditions are given by (Shikhmurzaev, 1993, 2006, 2007)

$$\mathbf{v}^s \cdot \mathbf{n} = 0, \quad (2)$$

$$p - \mu \mathbf{n} \cdot [\nabla \mathbf{u} + (\nabla \mathbf{u})^*] \cdot \mathbf{n} = \sigma \nabla \cdot \mathbf{n}, \quad (3)$$

$$\mu \mathbf{n} \cdot [\nabla \mathbf{u} + (\nabla \mathbf{u})^*] \cdot (\mathbf{I} - \mathbf{nn}) - \nabla \sigma = 0, \quad (4)$$

$$\rho \mathbf{u} \cdot \mathbf{n} = -(\rho^s - \rho_{1e}^s) \tau^{-1}, \quad (5)$$

$$\nabla \cdot (\rho^s \mathbf{v}^s) = -(\rho^s - \rho_{1e}^s) \tau^{-1}, \quad (6)$$

$$(1 + 4\alpha\beta) \nabla \sigma = 4\beta(\mathbf{v}^s - \mathbf{u}) \cdot (\mathbf{I} - \mathbf{nn}), \quad (7)$$

whereas on the solid surface moving parallel to itself with velocity \mathbf{U} , one has

$$\mathbf{v}^s \cdot \mathbf{n} = 0, \quad (8)$$

$$\mu \mathbf{n} \cdot [\nabla \mathbf{u} + (\nabla \mathbf{u})^*] \cdot (\mathbf{I} - \mathbf{nn}) - \frac{1}{2} \nabla \sigma = \beta(\mathbf{U} - \mathbf{u}) \cdot (\mathbf{I} - \mathbf{nn}), \quad (9)$$

$$\rho \mathbf{u} \cdot \mathbf{n} = -(\rho^s - \rho_{2e}^s) \tau^{-1}, \quad (10)$$

$$\nabla \cdot (\rho^s \mathbf{v}^s) = -(\rho^s - \rho_{2e}^s) \tau^{-1}, \quad (11)$$

$$\left[\mathbf{v}^s - \frac{1}{2}(\mathbf{u} + \mathbf{U}) \right] \cdot (\mathbf{I} - \mathbf{nn}) = \alpha \nabla \sigma. \quad (12)$$

Here, σ is the surface tension in the interfacial layer which is modelled as a 2D ‘surface phase’; ρ^s is the surface density in this phase (mass per unit area) and \mathbf{v}^s is the velocity with which it is transported along the interface; $\alpha, \beta, \gamma, \tau, \rho_{ie}^s (i = 1, 2)$ are phenomenological material constants; \mathbf{I} is the metric tensor; and the tensor $(\mathbf{I} - \mathbf{nn})$ singles out the tangential projection of a vector so that, e.g. $\mathbf{u} \cdot (\mathbf{I} - \mathbf{nn}) = \mathbf{u}_{\parallel}$.

The model has been established and examined in a number of works (Shikhmurzaev, 1993, 1994, 2006), so that here we will only briefly comment on the meaning of equations. On the free surface, in addition to the usual conditions on the normal and tangential stresses (3) and (4), the model takes into account mass exchange between the bulk and the surface phase (5) and (6) that takes place when the surface density ρ^s deviates from its equilibrium value ρ_{1e}^s . Similar to (5) and (6), conditions (10) and (11) describe mass exchange between the bulk and the liquid–solid interface. Importantly, the tangential components of the velocity in the surface phase \mathbf{v}^s , the bulk velocity evaluated on the liquid-facing side of interfaces \mathbf{u} and the velocity of the solid substrate \mathbf{U} are, in a general case, different due to the torques acting on the surface phase. On the free surface, the conditions relating tangential components of \mathbf{v}^s and \mathbf{u} are given by (7), whereas (9) and (12) related tangential components of \mathbf{v}^s , \mathbf{u} and \mathbf{U} on the solid boundary. It is assumed that the solid surface is impermeable for, and chemically inert with respect to, the fluid and there is no actual slip on the solid surface. Hence, condition (12) essentially has the form of a ‘Darcy law’ in the interfacial layer.

The equation of state in the surface phase that closes the set of equations (2–12) for the surface variables is taken in a simple ‘barotropic’ form linking the surface tension σ with the surface density

$$\sigma = \gamma (\rho_0^s - \rho^s), \quad (13)$$

where γ and ρ_0^s are phenomenological constants. This equation is the simplest way of accounting for the fact that the surface tension decreases from its equilibrium value $\sigma_{1e} = \sigma(\rho_{1e}^s)$ in the free surface to that in the liquid–solid interface, $\sigma_{2e} = \sigma(\rho_{2e}^s)$, when the interfacial layer becomes more compressed (or, more generally, less rarified) due to the action of intermolecular forces from the bulk phases that determine the equilibrium values of ρ^s . The dependence of phenomenological material constants on viscosity and their estimates for particular fluids have been obtained by analysing experiments on dynamic wetting available in the literature (Shikhmurzaev, 1993, 1997; Blake & Shikhmurzaev, 2002).

Distributions of the surface parameters along the interfaces are linked at the contact line via the mass and momentum balance conditions

$$\rho_1^s \mathbf{v}_1^s \cdot \mathbf{e}_1 + \rho_2^s \mathbf{v}_2^s \cdot \mathbf{e}_2 = 0, \quad (14)$$

$$\sigma_1 \cos \theta_d = \sigma_3 - \sigma_2, \quad (15)$$

where the subscripts 1 and 2 refer to the limiting values as one approaches the contact line along the free surface and the solid–liquid interface, respectively; \mathbf{e}_1 and \mathbf{e}_2 are unit normals to the contact line directed along the appropriate interfaces (Fig. 1) and σ_3 is the tangential component of the reaction force acting on the contact line from the solid substrate. For the cosine of the dynamic contact angle θ_d , one has $\cos \theta_d = \mathbf{e}_1 \cdot \mathbf{e}_2$. In equilibrium, the dynamic contact angle is related to the static one, θ_s , via the classical Young equation

$$\sigma_{1e} \cos \theta_s = \sigma_3 - \sigma_{2e} \quad (16)$$

that links the material constants σ_{1e} , σ_{2e} and σ_3 (or, alternatively, after using (13), ρ_{1e}^s , ρ_{2e}^s , ρ_0^s , γ , σ_3) and hence allows one to replace one of them with θ_s , which is a material constant characterizing the interaction of all three contacting media and a quantity relatively easy to measure in experiments.

The boundary conditions (2–15) make the surface phases and the contact line regular ‘elements’ of a fluid mechanical model. Importantly, in this model we have that θ_d is part of the solution, unlike the case of the so-called ‘slip models’, where θ_d is prescribed as a function of U and hence becomes a given input. (The slip models have to interpret the experimentally measured contact angle as an ‘apparent’ one (see Fig. 1) which then also becomes part of the solution, though dependent on an adjustable parameter, namely, the distance of the point where this angle is calculated from the contact line. However, as shown recently (Wilson *et al.*, 2006), even with this adjustable concept added, the slip models fail to describe experimental observations.)

It is important to emphasize that it is $\tau \neq 0$ that is at the core of the interface formation phenomenon and hence at the core the model we are using. Otherwise, the model would degenerate into the standard Navier slip model that has been used in many works and whose deficiencies, alongside those of other slip models, have been analysed in Shikhmurzaev (2006).

In order to model curtain coating, we need to formulate additional boundary conditions specifying this particular flow. After introducing a Cartesian coordinate system as shown in Fig. 1, for the bulk flow one can set the inlet velocity and thickness of the falling liquid sheet

$$\mathbf{u} = \mathbf{U}_* \quad \text{for } -h/2 \leq x \leq h/2, \quad y = H, \quad (17)$$

where the inlet velocity \mathbf{U}_* is assumed to be uniform and have only the y -component, together with boundary conditions far downstream, which we will set in a soft form

$$\frac{\partial \mathbf{u}(x, y)}{\partial x} \rightarrow 0 \quad \text{as } x \rightarrow +\infty, \quad 0 \leq y \leq \tilde{h}U_*/U, \quad (18)$$

where \tilde{h} is to be determined. For the surface variables, we will assume that at the top of the curtain the interfaces are in equilibrium, i.e.

$$\rho^s = \rho_{1e}^s, \quad \mathbf{v}^s = \mathbf{u} \quad \text{for } x = \pm h/2, \quad y = H, \quad (19)$$

and that far downstream along the solid surface, the liquid–solid interface tends to its equilibrium state

$$\rho^s \rightarrow \rho_{2e}^s \quad (x \rightarrow +\infty, y = 0). \quad (20)$$

Equations (1–15) and (17–20) fully specify the problem.

Using U , h , $\mu U h^{-1}$, σ_{1e} and ρ_0^s as scales for velocity, length, pressure, surface tension and the surface density, respectively, to bring (1–15) and (17–20) to a non-dimensional form, we have that the problem is characterized by the following set of similarity parameters:

$$\begin{aligned} \text{Ca} &= \frac{\mu U}{\sigma_{1e}}, \quad \text{Bo} = \frac{\rho g h^2}{\sigma_{1e}}, \quad \bar{\beta} = \frac{\beta U h}{\sigma_{1e}}, \quad A = \alpha \beta, \quad \lambda = \frac{\gamma \rho_0^s}{\sigma_{1e}}, \quad Q = \frac{\rho_0^s}{\rho U \tau}, \\ \epsilon &= \frac{U \tau}{h}, \quad \bar{\sigma}_3 = \frac{\sigma_3}{\sigma_{1e}}, \quad \bar{\rho}_{1e}^s = \frac{\rho_{1e}^s}{\rho_0^s}, \quad \theta_s, \quad \bar{U}_* = \frac{U_*}{U}, \quad \bar{H} = \frac{H}{h}. \end{aligned}$$

After introducing the stream function ψ ,

$$u_x = \frac{\partial \psi}{\partial y}, \quad u_y = -\frac{\partial \psi}{\partial x},$$

one arrives at a biharmonic equation $\nabla^4 \psi = 0$, which is convenient to split into two second-order equations

$$\nabla^2 \psi = \omega, \quad \nabla^2 \omega = 0, \quad (21)$$

where

$$\omega = \frac{\partial u_x}{\partial y} - \frac{\partial u_y}{\partial x}$$

is the value of the vorticity vector directed perpendicular to the plane of flow. Using the notation $\zeta = \nabla \cdot \mathbf{n}$ for the free surface curvature, we can write down the boundary condition in the following way.

On the free surface:

$$\lambda(1 - \rho^s) \frac{d\zeta}{ds} = \text{Bo } g_\tau - \text{Ca} \frac{\partial \omega}{\partial n} - 2\text{Ca} \frac{\partial^2}{\partial s^2} \frac{\partial \psi}{\partial n} - \text{Ca} \zeta \omega, \quad (22)$$

$$\text{Ca} \omega = 2\text{Ca} \frac{\partial^2 \psi}{\partial s^2} + 2\text{Ca} \zeta \frac{\partial \psi}{\partial n} + \lambda \frac{d\rho^s}{ds},$$

$$\frac{\partial \psi}{\partial s} = -Q(\rho^s - \bar{\rho}_{1e}^s), \quad \epsilon \frac{d(\rho^s v^s)}{ds} = -(\rho^s - \bar{\rho}_{1e}^s), \quad (23)$$

$$4\bar{\beta} \left(v^s + \frac{\partial \psi}{\partial n} \right) + \lambda(1 + 4A) \frac{d\rho^s}{ds} = 0, \quad (24)$$

and on the solid substrate:

$$\text{Ca } \omega = 2\text{Ca} \frac{\partial^2 \psi}{\partial s^2} + \frac{\lambda}{2} \frac{d\rho^s}{ds} - \bar{\beta} \left(\frac{\partial \psi}{\partial n} + 1 \right), \quad (25)$$

$$\frac{\partial \psi}{\partial s} = -Q(\rho^s - \bar{\rho}_{2e}^s), \quad \epsilon \frac{d(\rho^s v^s)}{ds} = -(\rho^s - \bar{\rho}_{2e}^s), \quad (26)$$

$$v^s + \frac{1}{2} \left(\frac{\partial \psi}{\partial n} - 1 \right) + \frac{A\lambda}{\beta} \frac{d\rho^s}{ds} = 0. \quad (27)$$

At the contact line, one has (14) and (15), i.e.

$$(\rho^s v^s)_1 = (\rho^s v^s)_2, \quad \sigma_1 \cos \theta_d = \bar{\sigma}_3 - \sigma_2, \quad (28)$$

whereas at the top of the curtain and far downstream, the boundary conditions (17–20) take the form

$$\frac{\partial \psi}{\partial n} = 0, \quad \psi = \bar{U}_*(x + 1/2) \quad (-1/2 < x < 1/2, y = \bar{H}), \quad (29)$$

$$\frac{\partial \psi}{\partial n}, \frac{\partial^2 \psi}{\partial n^2} \rightarrow 0 \quad \left(x \rightarrow \infty, 0 < y < \frac{\tilde{h}}{h} \bar{U}_* \right), \quad (30)$$

$$\rho^s = \bar{\rho}_{1e}^s, \quad v^s = \pm \bar{U}_* \quad (x = \mp 1/2, y = \bar{H}), \quad (31)$$

$$\rho^s \rightarrow \bar{\rho}_{2e}^s \quad (x \rightarrow \infty, y = 0). \quad (32)$$

In (22–27), $\partial/\partial n$, $\partial/\partial s$ and d/ds stand for differentiation with respect to the outward normal and the arc length s , measured anticlockwise in the direction of the tangent \mathbf{t} (Fig. 1), respectively, v^s is the only non-zero (i.e. tangential) component of the surface velocity and g_τ is the tangential component of the unit vector in the direction of gravity.

The characteristic feature of the problem (21–32) is that the dynamic contact angle, as introduced by (28), is determined by the distributions of the surface parameters along the interfaces. These distributions are coupled with the bulk variables through the boundary conditions thus making the dynamic contact angle a functional of the entire flow field. On the other hand, as is always the case in dynamic wetting problems, the dynamic contact angle itself determines the position of the contact line and, ultimately, the shape of the interfaces thus affecting the global flow field. This interplay between the bulk and the interfacial variables introduced via the modified boundary conditions changes all the familiar patterns of the standard hydrodynamics. For example, near the contact line for the steady problem, the interfaces are no longer coinciding with streamlines, and the boundary conditions (23) and (26) for the normal component of the bulk velocity depend on the distributions of the surface parameters along the interfaces. The interrelatedness of the flow parameters, the distributions of the surface variables and the shape of the flow domain make a numerical solution of the problem (21–32) rather difficult to obtain since, in addition to the known difficulties of computing free surface flows (e.g. Tsai & Yue, 1996), one has to pay special attention to properly resolve the surface distributions, especially near the contact line.

3. Implementation of the combined algorithm

Preliminary computations of (21–32) have shown that, as suggested by an asymptotic analysis of the interface formation model (Shikhmurzaev, 1993, 1994), the surface variables vary steeply only near

the contact line where the liquid–gas ‘surface phase’ turns into the liquid–solid one and the surface parameters have to relax to new equilibrium values over some relaxation length. This length is typically small compared with the characteristic size of the flow domain so that away from the contact line, the surface densities have their (constant) equilibrium values, the surface velocity is equal to the tangential component of the bulk velocity and the bulk variables satisfy the standard boundary conditions on the free surface,

$$\psi = \text{const}, \quad \omega = 2\xi \frac{\partial \psi}{\partial n}, \quad (33)$$

$$\frac{d\xi}{ds} = \text{Bo } g_\tau - \text{Ca} \frac{\partial \omega}{\partial n} - 2\text{Ca} \frac{\partial^2}{\partial s^2} \frac{\partial \psi}{\partial n} - \text{Ca} \xi \omega, \quad (34)$$

and the Navier condition,

$$\psi = \text{const}, \quad \text{Ca} \omega + \bar{\beta} \left(\frac{\partial \psi}{\partial n} + 1 \right) = 0, \quad (35)$$

on the solid boundary. For small $\text{Ca}/\bar{\beta}$, the Navier condition turns into no slip, $\partial \psi / \partial n = -1$, but, to avoid switching between boundary conditions of different types, we will use (35) in the far field, though for all physically realistic values of parameters, the result is that the no-slip condition is satisfied with a very high accuracy.

On the upper free surface, for all physically realistic values of parameters, the surface variables satisfy (33) and (34) with a very high accuracy so that one can use these conditions instead of (22–24), though numerical implementation of the latter causes no difficulties.

To implement the combined BIE-FE technique, it is convenient to split the computational domain into two regions, Ω_b (outer region) and Ω_c (inner region), see Fig. 2a. In Ω_c , where the surface variables vary steeply, the FEM is applied to (21–28), whereas in Ω_b we can use the BIEM applied to (21), (29), (30), and (33–35) together with $\rho^s \equiv \bar{\rho}_{1e}^s$, $\rho^s \equiv \bar{\rho}_{2e}^s$, and $v^s \equiv \mathbf{u} \cdot \mathbf{t}$ on the appropriate parts of the boundary. Conditions (31) and (32) transform into the corresponding matching conditions at points

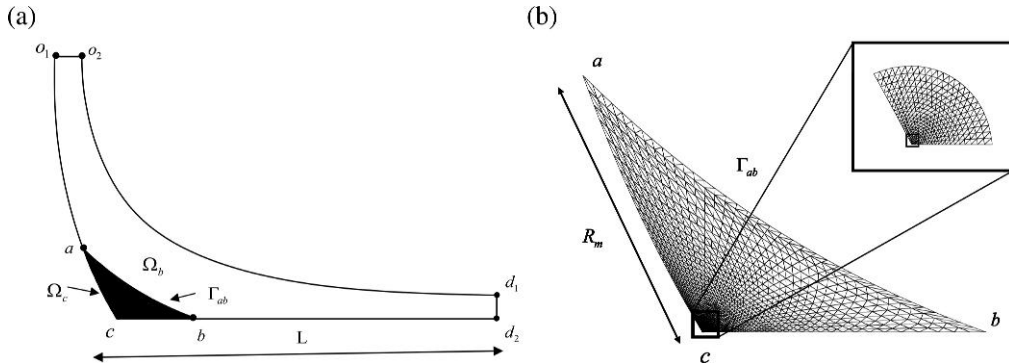


FIG. 2. (a) Sketch of the computational domain for curtain coating. (b) Computational domain in the corner region tessellated for the FEM. The blow-up of the mesh near the contact line is given in Fig. 3.

a and b . The bulk variables in the two regions are linked by the matching conditions

$$\psi_{\text{in}} = \psi_{\text{out}}, \quad \left(\frac{\partial \psi}{\partial n} \right)_{\text{in}} = - \left(\frac{\partial \psi}{\partial n} \right)_{\text{out}}, \quad (36)$$

$$\omega_{\text{in}} = \omega_{\text{out}}, \quad \left(\frac{\partial \omega}{\partial n} \right)_{\text{in}} = - \left(\frac{\partial \omega}{\partial n} \right)_{\text{out}} \quad (37)$$

we pose on the curve Γ_{ab} (numerical ‘internal interface’) separating Ω_b and Ω_c . In (36) and (37), the normal is pointing outwards with respect to the corresponding domain. The size of region Ω_c must be chosen in such a way that along the interfaces, its dimensions are large compared with the relaxation length for the surface variables. The main elements in implementing the combined algorithm are associated with the way of expressing (36–37) in terms of inner and outer variables, the shape and evolution of Γ_{ab} and the organization of the iteration procedure.

3.1 Boundary integral equation formulation

Using the Green’s theorem, the coupled form (21) of the biharmonic equation can be written down as a set of two integral equations for ψ , ω and their normal derivatives ψ_n , ω_n :

$$\begin{aligned} \eta(x_0)\psi(\mathbf{x}_0) &= \frac{1}{2\pi} \int_{\partial\Omega_b} \left\{ \psi(\mathbf{x})\mathbf{n} \cdot \nabla \ln r - \psi_n(\mathbf{x}) \ln r \right. \\ &\quad \left. + \frac{1}{4}\omega(\mathbf{x})\mathbf{n} \cdot \nabla (r^2 \ln r - r^2) - \frac{1}{4}\omega_n(\mathbf{x})(r^2 \ln r - r^2) \right\} dl, \quad (38) \\ \eta(x_0)\omega(\mathbf{x}_0) &= \frac{1}{2\pi} \int_{\partial\Omega_b} \{ \omega(\mathbf{x})\mathbf{n} \cdot \nabla \ln r - \omega_n(\mathbf{x}) \ln r \} dl, \end{aligned}$$

where $r = |\mathbf{x} - \mathbf{x}_0|$. The integrals are taken over the contour $\partial\Omega_b$ that confines region Ω_b . Where necessary, they must be interpreted in the principal value. The normal vector \mathbf{n} is pointed outwards the region Ω_b . The function $\eta(x)$ is given by

$$\eta(\mathbf{x}) = \begin{cases} 0, & \mathbf{x} \notin \Omega_b + \partial\Omega_b, \\ 1, & \mathbf{x} \in \Omega_b, \\ \frac{\alpha}{2\pi}, & \mathbf{x} \in \partial\Omega_b, \end{cases}$$

where α is the internal angle between the two tangents to $\partial\Omega_b$ on each side of \mathbf{x} .

To solve problem (38) numerically, we will use the classical BIEM formulation which has being applied successfully for decades to solve a variety of problems (e.g. [Jaswon & Symm, 1977](#); [Kelmanson, 1983a](#)). We will use as an illustration the simplest variant of the method. The domain boundary is subdivided into N smooth boundary elements $\partial\Omega_b = \sum_{j=1}^N \Delta\Omega_j$. On each element, the functions ψ , ψ_n , ω and ω_n are approximated by a step function, i.e. on the j th element

$$\begin{aligned} \psi(\mathbf{x}) &= \psi_j, & \psi_n(\mathbf{x}) &= \psi_{nj}, & \mathbf{x} &\in \Delta\Omega_j, \\ \omega(\mathbf{x}) &= \omega_j, & \omega_n(\mathbf{x}) &= \omega_{nj}, & \mathbf{x} &\in \Delta\Omega_j. \end{aligned} \quad (39)$$

This approximation is adequate for a large variety of Stokes flow problems, though for some problems a higher-order approximation is needed ([Pozrikidis, 1992](#)).

Using the discretized representation (39), system (38) takes the form

$$\begin{aligned} \eta(\mathbf{x}_0)\psi(\mathbf{x}_0) &= \frac{1}{2\pi} \sum_j \psi_j \int_{\Delta\Omega_j} \mathbf{n} \cdot \nabla \ln r \, dl - \frac{1}{2\pi} \sum_j \psi_{nj} \int_{\Delta\Omega_j} \ln r \, dl \\ &\quad + \frac{1}{8\pi} \sum_j \omega_j \int_{\Delta\Omega_j} \mathbf{n} \cdot \nabla (r^2 \ln r - r^2) dl - \frac{1}{8\pi} \sum_j \omega_{nj} \int_{\Delta\Omega_j} (r^2 \ln r - r^2) dl, \end{aligned} \quad (40)$$

$$\eta(\mathbf{x}_0)\omega(\mathbf{x}_0) = \frac{1}{2\pi} \sum_j \omega_j \int_{\Delta\Omega_j} \mathbf{n} \cdot \nabla \ln r \, dl - \frac{1}{2\pi} \sum_j \omega_{nj} \int_{\Delta\Omega_j} \ln r \, dl. \quad (41)$$

Equations (40) and (41) are then collocated at the midpoints of each interval $\mathbf{x}_0 \in \Delta\Omega_j$, $j = 1, \dots, N$, resulting in a system of $2N$ algebraic equations for $4N$ unknowns. All geometrical characteristics of the surface profile in (40) and (41) and in the boundary conditions, i.e. \mathbf{n} and ζ , are calculated at the midpoints of each interval on the basis of a cubic spline.

In a standard situation, to get a unique solution one would just set any two independent combinations of the variables ψ , ψ_n , ω , ω_n on the boundary. In terms of the number of unknowns, one needs to leave $2N$ unknown values after prescribing $2N$ known values on the boundary. In our case, $2N$ equations specifying the latter have different form on different parts of the boundary. On the free surface (contour $o_1 - a$ and $d_1 - o_2$), one has

$$\omega = 2\zeta \frac{\partial \psi}{\partial n} \quad (42)$$

together with $\psi = 0(o_1 - a)$ or $\psi = \bar{U}_*(d_1 - o_2)$. On the solid substrate (contour $b - d_2$), the Navier condition applies

$$\psi = \psi(\mathbf{x}_b), \quad \text{Ca} \omega + \bar{\beta} \left(\frac{\partial \psi}{\partial n} + 1 \right) = 0. \quad (43)$$

Note that, since in the region Ω_c the boundary is not a streamline due to adsorption–desorption processes on the interfaces, the value of the stream function on $c - d_2$ is, generally, not equal to zero. The inlet boundary conditions (29) can be implemented in different equivalent forms. It has been found that a convenient way of setting up a uniform flow is to use $\psi_n = 0$, $\omega_n = 0$ on $o_2 - o_1$ since this condition allows for self-corrections in the course of iterations. The uniform flow far downstream can be set up in a similar way. Control computations have been performed with conditions (29) and (30) implemented explicitly. The length L of the film in the downward direction (Fig. 2a) was chosen sufficiently large to guarantee the full recovery of the uniform flow downstream along the solid substrate and to ensure that there is no influence of the position of the contour $d_2 - d_1$ on the computational results.

In our BIEM formulation so far, no conditions have been imposed on the contour Γ_{ab} . This means that at the moment, we have $2N_B$ equations for $2N_B + 2N_{ab}$ unknowns, where N_B is the total number of intervals on $\partial\Omega_b$ and N_{ab} is the number of intervals on Γ_{ab} . After calculating all the kernel integrals and applying the conditions formulated above, system (40) and (41) can be represented in a matrix form as

$$\mathbf{A}_{\text{BIE}} \mathbf{f}_{\text{BIE}} = \mathbf{B}_{\text{BIE}}, \quad (44)$$

where the solution vector \mathbf{f}_{BIE} has the length $2N_B + 2N_{ab}$ and \mathbf{A}_{BIE} is a $2N_B \times (2N_B + 2N_{ab})$ matrix. All non-singular kernel integrals in (40) and (41) are taken numerically by means of a standard 20-point

Gaussian quadrature with double precision numerical accuracy. On the intervals where $\mathbf{x} - \mathbf{x}_0 = 0$ occurs, the kernel integrals are taken analytically in a similar way as in [Kelmanson \(1983a\)](#).

3.2 Finite-element representation

The solution in \mathcal{Q}_c is obtained using a Galerkin-weighted finite-element technique. The domain is tessellated into contiguous three-node triangular elements (Figs 2b and 3). The size of the elements is gradually increasing by 3–8% while moving radially from the contact line to account for the natural length scales of the problem (Fig. 2b). Each element in the physical space is mapped onto the standard ‘master’ element with the local coordinate basis (χ, η) (Fig. 4) by means of the linear transformation

$$\mathbf{x}(\chi, \eta) = \sum_{i=1}^3 \mathbf{x}_i \Phi_i(\chi, \eta), \quad (45)$$

where

$$\Phi_1(\chi, \eta) = 1 - \chi - \eta, \quad \Phi_2(\chi, \eta) = \chi, \quad \Phi_3(\chi, \eta) = \eta \quad (46)$$

and $\mathbf{x}_i = (x_i, y_i)$ are the coordinates of the element’s nodes in the physical space. Then, on the ‘master’ element, functions ψ and ω are approximated by the same linear shape functions Φ_i through the nodal values ψ_i, ω_i :

$$\psi(\chi, \eta) = \sum_{i=1}^3 \psi_i \Phi_i(\chi, \eta), \quad \omega(\chi, \eta) = \sum_{i=1}^3 \omega_i \Phi_i(\chi, \eta). \quad (47)$$

The approach is similar to that reported in [Peeters *et al.* \(1987\)](#) and [Gaskell *et al.* \(1999\)](#), where second-order elements were used. Here, we use linear elements as an illustration and a benchmark for the higher-order schemes; as for the BIEM, an increase of the order of approximation is technically straightforward.

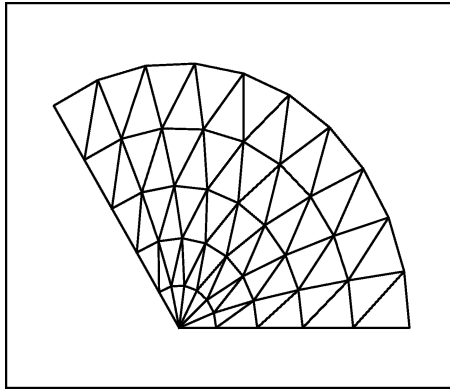


FIG. 3. Blow-up of the corner region down to the last finite element. The spatial resolution in the transversal direction is not important for the final solution since, as shown asymptotically in [Shikhmurzaev \(2006\)](#) and confirmed by our computations, near the contact line it is a uniform flow; however, it is crucial for the convergence of the code.

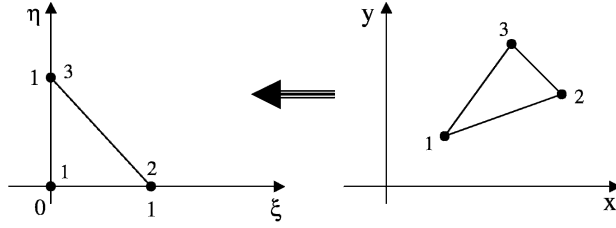


FIG. 4. Left: The ‘master’ element, with local coordinate basis (χ, η) , which is used to derive the FEM equations. Right: A general element in the physical space; the element is mapped onto the ‘master’ element by means of the linear transformation (45). For both elements, the numbered black circles are the nodes at which the stream function and vorticity are calculated.

The system (21) can be written in a weak form using Φ_i as weighting functions as follows:

$$\int_{\Omega_c} \nabla \Phi_i \nabla \psi \, d\Omega + \int_{\Omega_c} \Phi_i \omega \, d\Omega - \int_{\partial\Omega_c} \Phi_i \psi_n \, ds = 0, \quad (48)$$

$$\int_{\Omega_c} \nabla \Phi_i \nabla \omega \, d\Omega - \int_{\partial\Omega_c} \Phi_i \omega_n \, ds = 0, \quad (49)$$

where the integrals over the domain boundary $\partial\Omega_c$ must be dropped since equations for the boundary nodes are replaced by the weak formulation of the appropriate boundary conditions.

On the boundary, for each element, the surface variables ρ^s and v^s are approximated using 1D shape functions $A_i(\vartheta)$:

$$\rho^s(\vartheta) = \sum_{i=1}^2 \rho_i^s A_i(\vartheta), \quad v^s(\vartheta) = \sum_{i=1}^2 v_i^s A_i(\vartheta), \quad (50)$$

where

$$A_1 = 1 - \vartheta, \quad A_2 = \vartheta, \quad 0 \leq \vartheta \leq 1. \quad (51)$$

One may note that the set of functions (51) is actually a projection of the set (46) onto an element boundary. For example, the set (46) on the boundary $(0 < \chi < 1, \eta = 0)$, between nodes $\chi = 0, \eta = 0$ and $\chi = 1, \eta = 0$, becomes

$$\Phi_1(\chi, \eta) = 1 - \chi, \quad \Phi_2(\chi, \eta) = \chi, \quad \Phi_3(\chi, \eta) = 0. \quad (52)$$

That is, identifying χ with ϑ , one has

$$\Phi_1 = A_1, \quad \Phi_2 = A_2.$$

All the boundary conditions used in the FE part of the code are transformed into a weak formulation using the set (51) as weighting functions. On the free surface from (22) to (24), one has

$$\int_{\partial\Omega} A_i \left\{ \omega + 2Q \frac{d\rho^s}{ds} - 2\xi \psi_n - \frac{\lambda}{Ca} \frac{d\rho^s}{ds} \right\} ds = 0, \quad (53)$$

$$\int_{\partial\Omega} A_i \left\{ \frac{\partial\psi}{\partial s} + Q(\rho^s - \bar{\rho}_{1e}) \right\} ds = 0, \quad (54)$$

$$\int_{\partial\Omega} A_i \left\{ \epsilon \frac{d(\rho_{(0)}^s v^s)}{ds} + Q(\rho^s - \bar{\rho}_{1e}) \right\} ds = 0, \quad (55)$$

$$\int_{\partial\Omega} A_i \left\{ 4\bar{\beta}(v^s + \psi_n) + (1 + 4A)\lambda \frac{d\rho^s}{ds} \right\} ds = 0. \quad (56)$$

Similarly, on the solid boundary we have

$$\int_{\partial\Omega} A_i \left\{ \omega + 2Q \frac{d\rho^s}{ds} - \frac{\lambda}{2Ca} \frac{d\rho^s}{ds} + \frac{\bar{\beta}}{Ca} (\psi_n + 1) \right\} ds = 0, \quad (57)$$

$$\int_{\partial\Omega} A_i \left\{ \frac{\partial\psi}{\partial s} + Q(\rho^s - \bar{\rho}_{2e}) \right\} ds = 0, \quad (58)$$

$$\int_{\partial\Omega} A_i \left\{ \epsilon \frac{d(\rho_{(0)}^s v^s)}{ds} + Q(\rho^s - \bar{\rho}_{2e}) \right\} ds = 0, \quad (59)$$

$$\int_{\partial\Omega} A_i \left\{ \bar{\beta} \left(v^s + \frac{1}{2}(\psi_n - 1) \right) + A\lambda \frac{d\rho^s}{ds} \right\} ds = 0. \quad (60)$$

The non-linear terms in (23) and (26), and consequently in (55) and (59), have been linearized to use an iterative procedure. As an initial guess, it was sufficient to set $\rho_{(0)}^s$ to its equilibrium value on each surface $\rho_{(0)}^s = \bar{\rho}_{1,2e}^s$.

The surface shape and its curvature have been approximated by means of a cubic spline. In the weak formulation, on the boundary of each element, the curvature is approximated using the set of functions A_i through the nodal boundary values ζ_i obtained from the spline procedure, i.e. $\zeta(\vartheta) = \sum_{i=1}^2 \zeta_i A_i(\vartheta)$.

Now, to match solutions in regions Ω_c and Ω_b one needs to use conditions (36) and (37) on Γ_{ab} . They can be written down in the weak form as follows:

$$\int_{\partial\Omega} A_i \{ \psi_{\text{in}} - \psi_{\text{out}} \} ds = 0, \quad \int_{\partial\Omega} A_i \left\{ \left(\frac{\partial\psi}{\partial n} \right)_{\text{in}} + \left(\frac{\partial\psi}{\partial n} \right)_{\text{out}} \right\} ds = 0, \quad (61)$$

$$\int_{\partial\Omega} A_i \{ \omega_{\text{in}} - \omega_{\text{out}} \} ds = 0, \quad \int_{\partial\Omega} A_i \left\{ \left(\frac{\partial\omega}{\partial n} \right)_{\text{in}} + \left(\frac{\partial\omega}{\partial n} \right)_{\text{out}} \right\} ds = 0. \quad (62)$$

In (61) and (62), the variables in the inner region, ψ_{in} and ω_{in} , are represented by means of the set of functions $A_i(\vartheta)$, i.e. on each interval, e.g. for ψ_{in} , one has

$$\psi_{\text{in}}(\vartheta) = \sum_{i=1}^2 \psi_i^{\text{in}} A_i(\vartheta),$$

whereas the variables ψ_{out} , ω_{out} , $\partial\psi/\partial n_{\text{out}}$ and $\partial\omega/\partial n_{\text{out}}$ in the outer region are approximated by the representation (39) used in the BIEM, i.e. on each interval $\Delta\Omega_j$ one has, e.g. for ψ_{out} and $(\omega_n)_{\text{out}}$,

$$\psi_{\text{out}} = \psi_j^{\text{out}}, \quad \left(\frac{\partial\omega}{\partial n} \right)_{\text{out}} = (\omega_n^{\text{out}})_j.$$

It is worth emphasizing here that the shape and position of the contour Γ_{ab} should be chosen, on the one hand, with some caution and, on the other, that this choice can substantially reduce computation costs. To avoid degeneration of the finite elements comprising the points x_a and x_b , the angle θ_{ab} at which Γ_{ab} meets the free surface and the solid substrate at points x_a and x_b should be about 30° and kept constant during iterations (here θ_{ab} is measured through Ω_c). Higher values of θ_{ab} increase the local error of the BIEM, whereas much lower values do the same with the accuracy of the FEM. The position of the contour can be chosen using the asymptotic estimates for the actual relaxation length for the surface variables $l_r = k_\rho^{-1}$ (see (71)) such that $R_m \simeq 20\text{--}30l_r$. This allows one to avoid tessellation of large parts of the domain and, on the other hand, ensures complete relaxation of the surface variables to their equilibrium values.

Alternatively, the matching of the FEM and the BIEM can be performed by using two curves, Γ'_{ab} and Γ''_{ab} , that make regions Ω_b and Ω_c overlap. This way of matching removes the above restrictions on the shape of Γ_{ab} at the expense that now the curve lying inside Ω_c is no longer formed by the sides of the finite elements, and one has to apply a suitable interpolation procedure to implement the matching conditions.

Equations (48), (49) and (53–62) provide a weak formulation of the problem in the inner region Ω_c . To complete the formulation, we have to add algebraic boundary condition at the contact line (28), set the surface density at points a and b to equilibrium values,

$$\rho_1^s(\mathbf{x}_a) = \bar{\rho}_{1e}^s, \quad \rho_2^s(\mathbf{x}_b) = \bar{\rho}_{2e}^s, \quad (63)$$

and set the stream function and the surface velocity to their initial values at \mathbf{x}_a ,

$$\psi(\mathbf{x}_a) = 0 \quad (64)$$

and, according to (31),

$$v^s(\mathbf{x}_a) + \psi_n(\mathbf{x}_a) = 0. \quad (65)$$

Then, in the assembly procedure, the integration of the residual equations (48), (49) and (53–62) is achieved on an element-by-element basis using the ‘master’ element with local coordinate basis (χ, η) and transformation (45) by means of standard Gaussian quadrature to form a system of algebraic equations. For example, during the assembly procedure, (48) is integrated on each physical element m as follows:

$$\Psi_j \int \nabla \Phi_i \nabla \Phi_j J^m(\chi, \eta) d\chi d\eta + \omega_j \int \Phi_i \Phi_j J^m(\chi, \eta) d\chi d\eta = 0, \quad (66)$$

where $j = 1, \dots, 3$ and $i = 1, \dots, 3$ are the node numbers, and $J^m(\chi, \eta) = \partial(x, y)/\partial(\chi, \eta)$ is the Jacobian of transformation (45), i.e. the actual integration is performed over the ‘master’ element. The procedure is carried out for each element in Ω_c and the results are assembled to form a system of linear equations. The actual assembly procedure is standard (see, e.g. Gresho & Sani, 2000), and below we only outline key elements relevant to our particular case.

First of all, (48) and (49) are integrated for all elements in Ω_c resulting in a system of $2N_c$ algebraic equations, N_c is the number of nodes in Ω_c . Then, boundary conditions are integrated for each element located on the relevant boundary of Ω_c . Namely, (53) and (54) are integrated on the free surface, (57) and (58) are integrated on the solid substrate and finally (61) are integrated on Γ_{ab} . The algebraic equations obtained from the integration of boundary conditions (53), (54), (57), (58) and (61) then replace the corresponding algebraic equations obtained from (48) and (49) at the nodal points located

on the particular boundary. The other algebraic equations resulting from the integration of conditions (55), (56), (59), (60) and (62) are added to the system to form in total a system of N_{t1} linear equations for N_{t2} unknowns, where $N_{t1} = 2N_c + 2N_{fs} + 2N_{ss} + 2N_{ab}$, $N_{t2} = 2N_c + 2N_{fs} + 2N_{ss}$ and N_{fs} , N_{ss} are the number of nodes on the free surface and the solid substrate, respectively. Finally, algebraic boundary conditions (63–65) must be applied. They replace equations at nodes x_a and x_b for each variable ρ^s , ψ and v^s , respectively.

After completing the assembly procedure, the result can be presented in a matrix form as

$$\mathbf{A}_{\text{FEM}} \mathbf{f}_{\text{FEM}} = \mathbf{B}_{\text{FEM}}, \quad (67)$$

where \mathbf{A}_{FEM} is a $(N_{t1} \times N_{t2})$ matrix and \mathbf{f}_{FEM} is a solution vector of length N_{t2} .

Combining (44) and (67), one has in total a system of $2N_B + 2N_c + 2N_{fs} + 2N_{ss} + 2N_{ab}$ linear equations for the same number of unknowns or

$$\mathbf{A}_{\text{Hyb}} \mathbf{f}_{\text{Hyb}} = \mathbf{B}_{\text{Hyb}}. \quad (68)$$

Matrix \mathbf{A}_{Hyb} has a hybrid structure: the part of the matrix resulting from the FEM is sparse, whereas the one coming from the BIEM is full. The matrix is stored in a sparse coordinate format and then inverted by the LU factorization with an iterative refinement.

3.3 Computation of the free surface profiles

Free surface profiles in the problem are determined iteratively from boundary condition (22) which is considered as a second-order differential equation for the angle θ formed by the tangential unit vector \mathbf{t} to the x -axis (Fig. 1):

$$\lambda(1 - \rho^s) \frac{d\xi}{ds} = \text{Bo } g_\tau - \text{Ca } \omega_n - 2\text{Ca} \frac{\partial^2 \psi_n}{\partial s^2} - \text{Ca } \xi \omega, \quad \xi = \frac{d\theta}{ds}. \quad (69)$$

At each step of the iterations, (69) are solved with two boundary conditions and given distributions of ψ_n , ω , ω_n , ρ^s and g_τ along the surface. The boundary conditions are

$$\begin{aligned} \theta_{d_1} &= \pi, & \theta_{o_2} &= \pi/2, & \text{on } d_1 - o_2, \\ \theta_{o_1} &= 3\pi/2, & \theta_c &= \pi + \theta_d, & \text{on } o_1 - c. \end{aligned}$$

Once new function $\theta(s)$ is obtained, new surface profile is calculated from a system

$$\frac{dx}{ds} = \cos \theta, \quad \frac{dy}{ds} = \sin \theta$$

with initial conditions

$$\begin{aligned} x(s_{o_2}) &= 1/2, & y(s_{o_2}) &= \bar{H}, & \text{on } d_1 - o_2, \\ x(s_{o_1}) &= -1/2, & y(s_{o_1}) &= \bar{H}, & \text{on } o_1 - c. \end{aligned}$$

Since in an iterative procedure, in a general case, one has $y(s_c) \neq 0$ and $x(s_{d_1}) \neq L$, we have to rescale the new profiles

$$\begin{aligned} x'(s) &= x(s_{o_2}) + (x(s) - x(s_{o_2})) \frac{(L - x(s_{o_2}))}{(x(s_{d_1}) - x(s_{o_2}))}, \\ y'(s) &= y(s_{o_1}) - (y(s) - y(s_{o_1})) \frac{y(s_{o_1})}{(y(s_c) - y(s_{o_1}))} \end{aligned}$$

to ensure that for them $y'(s_c) = 0$ and $x'(s_{d_1}) = L$. The iterations are terminated when the following criterion is satisfied:

$$\max_{i=1, \dots, N} |\mathbf{x}'(s'_i) - \mathbf{x}(s_i)| \leq 0.01,$$

where N is the number of points on the boundary and s' is the arc length calculated on the new profile \mathbf{x}' .

4. Flow in the corner region

Before applying the combined algorithm in full, its most essential, and in terms of the boundary conditions, new component, the FE code, has been tested for the flow in a corner region Ω_c where, for some limiting cases, analytical solutions are available.

Although the set of boundary conditions (22–27) looks rather complicated, in some asymptotic limits one can arrive at analytical results for the velocity dependence of the contact angle that can be used as a benchmark for the code. One of such results is the steady flow at $\text{Ca} \ll 1$ for a fluid where $\lambda \gg 1$ (Shikhmurzaev, 1994). In this limit, the ‘moving contact line problem’ becomes a local one and the free surface near the contact line is, to leading order, planar so that one can consider the contact angle as a feature determined by the prescribed outer flow.

To consider the flow in a corner region (Fig. 2b) computationally on the outer boundary of this region, we use the stream function and vorticity distributions from Moffatt (1964),

$$\psi_M = \frac{r((\theta - \theta_d) \sin \theta - \theta \cos \theta_d \sin(\theta - \theta_d))}{\sin \theta_d \cos \theta_d - \theta_d}, \quad \omega_M = \frac{\cos \theta - \cos \theta_d \cos(\theta - \theta_d)}{r(\sin \theta_d \cos \theta_d - \theta_d)}, \quad (70)$$

as in the asymptotic solution. Using the size of the corner region as a characteristic length scale of the flow domain h , we can rewrite the asymptotic solution for the surface density in the form

$$\rho_1^s = \bar{\rho}_{1e}^s, \quad \rho_2^s = \bar{\rho}_{2e}^s - C_\rho \lambda^{-1} \exp(-k_\rho r), \quad (71)$$

where

$$\begin{aligned} k_\rho &= 2V\epsilon^{-1}(\bar{\rho}_{2e}^s)^{-1}[\sqrt{V^2 + \bar{\rho}_{2e}^s} - V], \quad C_\rho = \frac{2V\lambda(\bar{\rho}_{2e}^s + \bar{\rho}_{1e}^s u_d)}{(\bar{\rho}_{2e}^s + V^2)^{1/2} + V}, \\ u_d &= \frac{\sin \theta_d - \theta_d \cos \theta_d}{\sin \theta_d \cos \theta_d - \theta_d}, \quad V^2 = \frac{\epsilon \bar{\beta}}{\lambda(1 + 4A)}, \quad \bar{\rho}_{2e}^s = 1 - \frac{\bar{\sigma}_3}{\lambda} + \frac{\cos \theta_s}{\lambda}. \end{aligned}$$

The resulting dependence of the contact angle on the contact line speed is given by

$$\cos \theta_s - \cos \theta_d = \frac{2V\lambda(\bar{\rho}_{2e}^s + \bar{\rho}_{1e}^s u_d)}{(\bar{\rho}_{2e}^s + V^2)^{1/2} + V}. \quad (72)$$

The results of comparing the numerical solution with (71) and (72) are summarized in Figs 5–7. Figures 5 and 6 show the dependence of the surface density on the distance from the contact line at different values of the substrate velocity, i.e. for the capillary numbers $\text{Ca} = 10^{-3}$ and $\text{Ca} = 10^{-2}$. As one can see, the numerical solution matches the asymptotic one with the accuracy of $\Delta\rho^s/\rho^s \simeq 5 \times 10^{-4}$ to 3×10^{-3} . Given that, unlike the leading-order asymptotics in Ca as $\text{Ca} \rightarrow 0$, the code fully accounts for the influence of the bulk flow on the distributions of the surface parameters, one should expect the difference between the numerical and the asymptotic results being proportional to Ca . This difference goes down indeed as the capillary number decreases. For low capillary numbers, the difference between the numerical and the analytical results is due essentially to the limited spatial resolution of the code in these runs where for $N_c = 2420$, $N_{fs} = N_{ss} = 110$, we had just $N_{rl} = 85$ mesh points over the length of $3l_r$ ($l_r = k_\rho^{-1}$ is the actual relaxation length). The tested accuracy of the code in calculating

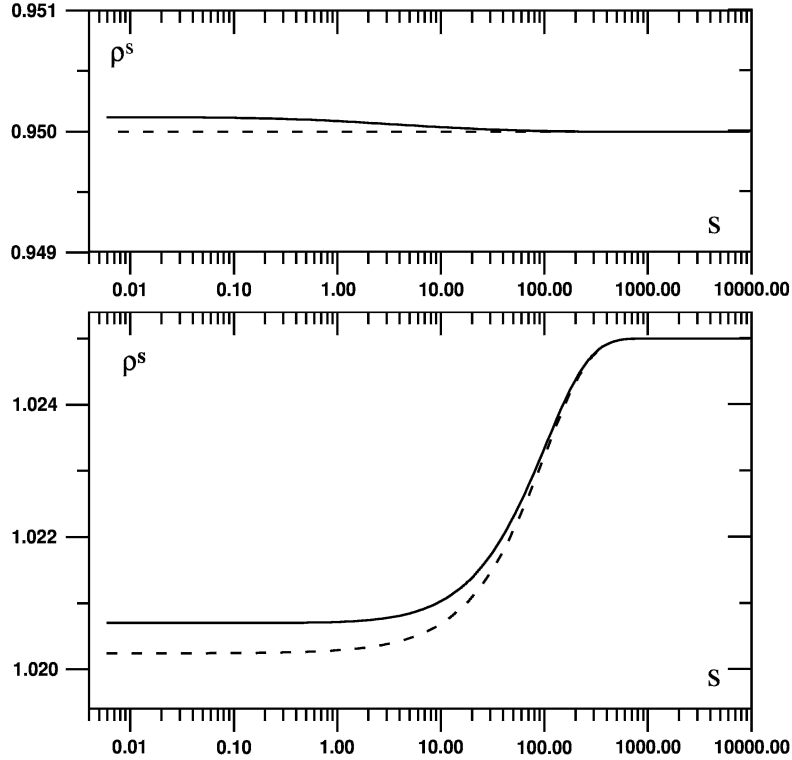


FIG. 5. The distribution of the surface density along the free surface (top) and along the liquid–solid interface (bottom) in the corner flow for $\text{Ca} = 0.001$, $\theta_s = 60^\circ$, $\lambda = 20$, $\bar{\beta} = 25$, $Q = 0.4$, $\epsilon = 10^{-4}$ and $A = 1$. The asymptotic distribution, (71), is shown by the dashed line. The data point corresponding to $s = 0$ and a few neighbouring points are taken out.

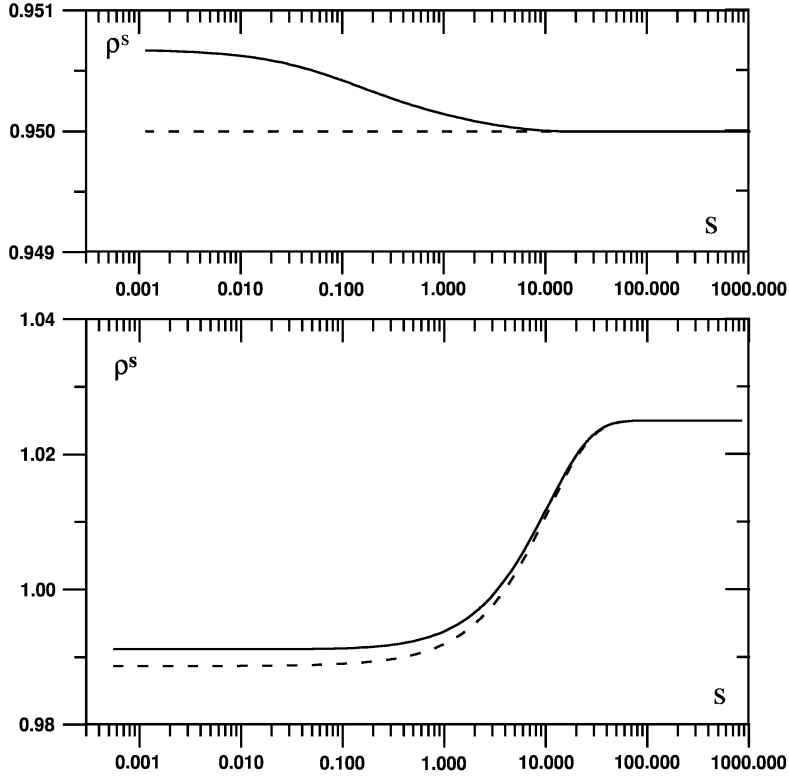


FIG. 6. The distribution of the surface density along the free surface (top) and along the liquid–solid interface (bottom) in the corner flow for $Ca = 0.01$, $\theta_s = 60^\circ$, $\lambda = 20$, $\bar{\beta} = 250$, $Q = 0.04$, $\epsilon = 10^{-3}$ and $A = 1$. The asymptotic distribution, (71), is shown by the dashed line. The distance s from the contact line is scaled with $U\tau$; the data point corresponding to $s = 0$ and a few neighbouring points are taken out.

the contact angle is consistent with the estimated error given by

$$\Delta\theta_d \simeq \Delta\rho^s \lambda$$

and was about 0.5° – 1° at $\lambda = 20$. This value is in a good agreement with the observed deviation of the dynamic contact angle calculated numerically from the asymptotic value (Fig. 7).

The convergence of the solution illustrated in Fig. 8 suggests that the number of mesh points $N_c = 2420$ is sufficient for most applications. It should be noted, though, that for higher values of $Ca \sim O(1)$, the approximation error is expected to increase, and a better spatial resolution (or/and a higher order of approximation) is required to keep the accuracy within $\Delta\theta_d \simeq 0.5^\circ$ – 1° .

5. Simulations of curtain coating

In this section, we will give some results illustrating the performance of the combined algorithm in the simulations of curtain coating in the parameter range relevant to the water–glycerol solutions used in experiments as a convenient test fluid. Using characteristic physical parameters of the water–glycerol solutions and estimates of the phenomenological material constants of the model α , β , γ , τ , ρ_0^s and

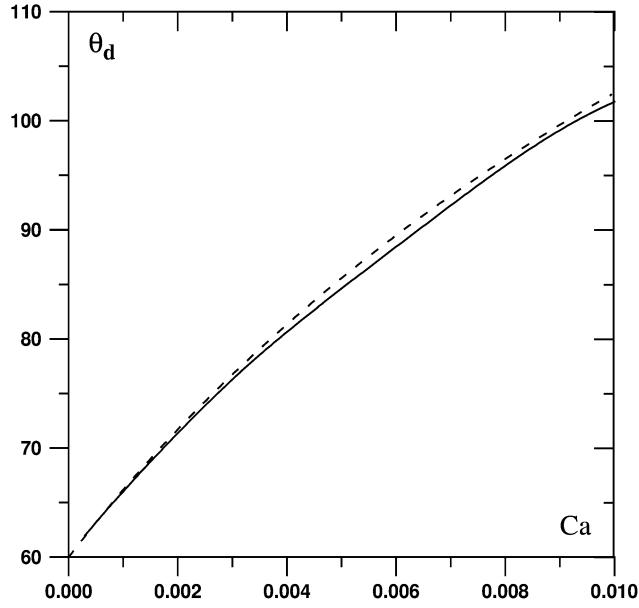


FIG. 7. The dependence of the dynamic contact angle on the substrate velocity U (shown as the dependence on Ca) in the corner flow for $\lambda = 20$ and $\theta_s = 60^\circ$. Other parameters scaled with U ($\bar{\beta}$, Q and ϵ) were changing accordingly. The asymptotic dependence, (72), is shown by the dashed line.

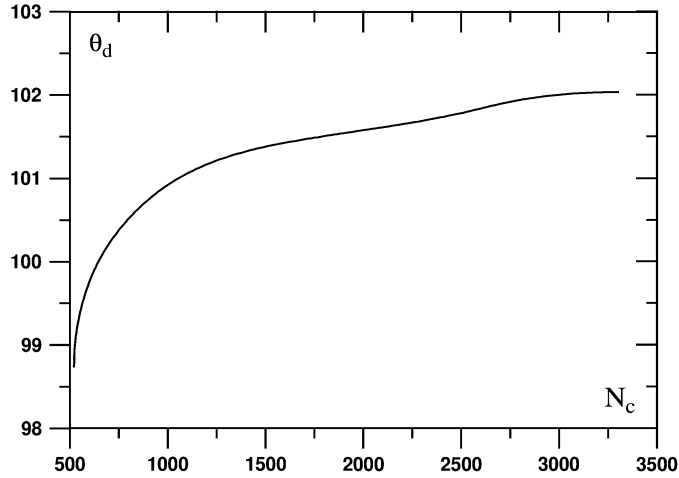


FIG. 8. The dependence of the dynamic contact angle calculated numerically for the corner flow on the total number of mesh points at $Ca = 0.01$; the number of mesh points over the length $3l_r$ increases proportionally. Other parameters are the same as in Fig. 6.

ρ_{je} , $j = 1, 2$, obtained in [Blake & Shikhmurzaev \(2002\)](#), we calculate steady curtain profiles and the corresponding distributions of the variables for different values of the substrate velocity U . Variations of the substrate velocity simultaneously change several non-dimensional parameters (Ca , $\bar{\beta}$, Q , \bar{U}_* and ϵ), whereas other parameters (Bo , A , λ , $\bar{\sigma}_3$, $\bar{\rho}_{1e}$, \bar{H} and θ_s) remain fixed. (For the analysis of the role played

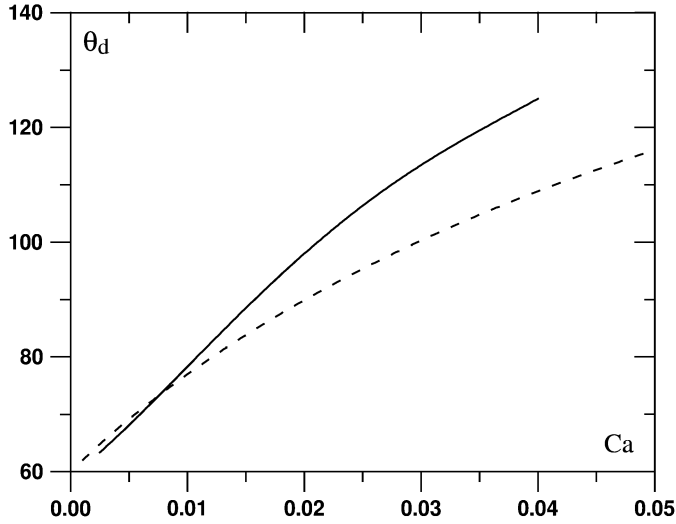


FIG. 9. Dependence of the dynamic contact angle in the curtain coating on U (shown as the dependence on Ca). Here, $\bar{U}_* = 1$; other non-dimensional parameters scaled with U ($\bar{\beta}$, \bar{Q} and ϵ) were changing accordingly. The asymptotic dependence for the corner flow, (72), is shown by the dashed line.

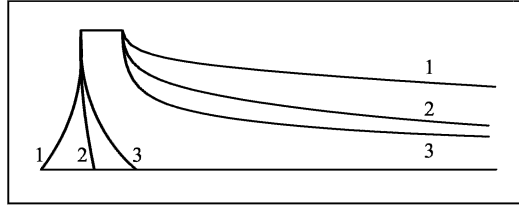


FIG. 10. Typical profiles of the curtain for different contact line speeds. Here, $\bar{U}_* = 1$, $\theta_s = 60^\circ$ and $\bar{H} = 5$; 1: $Ca = 0.0025$; 2: $Ca = 0.02$; 3: $Ca = 0.04$; other non-dimensional parameters scaled with U ($\bar{\beta}$, \bar{Q} and ϵ) change accordingly. In the horizontal direction, the plot is clipped at approximately 0.1 of the actual size of the computational domain.

by the dimensionless parameters, see [Lukyanov & Shikhmurzaev, 2006.](#)) In our test simulations, we use $A = 1$, $\lambda = 2.5$, $\bar{\sigma}_3 = 0$, $\bar{\rho}_{1e} = 0.6$, $\bar{H} = 5$, $\theta_s = 60^\circ$ and keep $U_* = 1$. Although for the typical flow conditions the code is intended to describe the Bond number is small, $Bo \simeq 2.5 \times 10^{-5}$, in the computations we chose to keep the body force term in (22) as a stabilizing factor for the film far downstream the solid substrate. The numerical resolution of the combined method was taken at the level sufficient to ensure that the accuracy of the contact angle is about $\sim 1.5^\circ - 2^\circ$ in all the runs, i.e. $N_B = 680$, $N_C = 3010$ with $N_{rl} = 80$ over the distance $3l_r$. Note that while the actual relaxation length l_r was changing with Ca , the spatial resolution in that region, i.e. the number of points N_{rl} , was kept the same.

The results of our simulations are summarized in Figs 9–13. In Fig. 9, the dynamic contact angle θ_d is shown as a function of the capillary number Ca . Remarkably, as $Ca \rightarrow 0$, the contact angle is getting close to the values predicted by the asymptotic solution (72) even though, in this case, the parameter $\lambda \sim O(1)$, whereas the asymptotics was obtained for $\lambda \gg 1$. At higher values of the substrate velocity, as one should anticipate, the dependence diverges from the asymptotic one. The reason for this effect

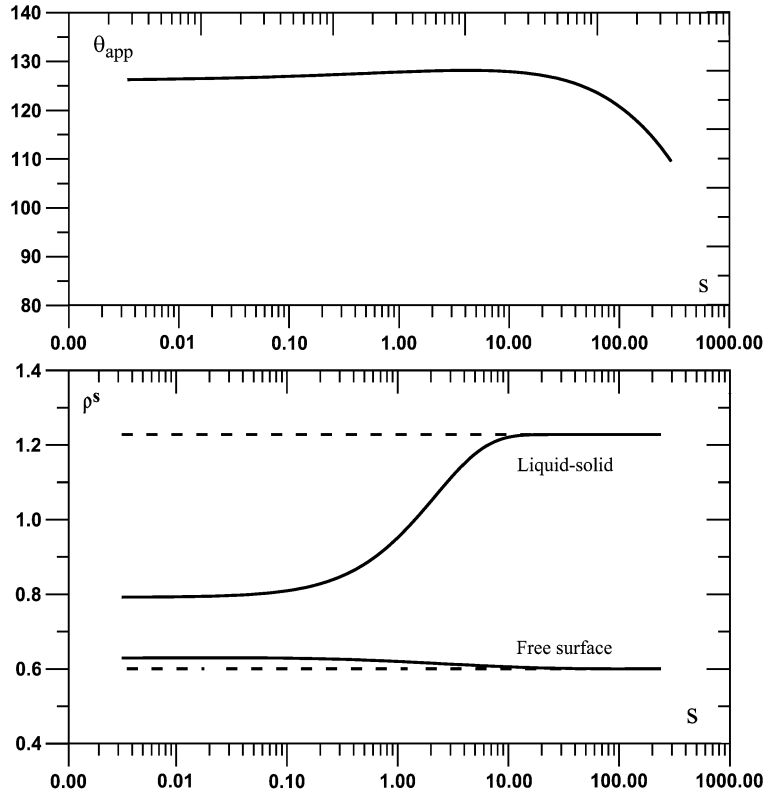


FIG. 11. Apparent contact angle θ_{app} and the distribution of the surface density ρ^s in curtain coating for $Ca = 0.04$. The equilibrium values of the surface density are shown by the dashed line.

is that the terms proportional to Ca in the boundary conditions are, to leading order, neglected in the asymptotics, whereas in the code they are fully taken into account and, as Ca increases, so does the influence of the bulk flow on the surface parameters distribution that ultimately influences the contact angle.

The corresponding curtain profiles and distributions of the surface density are shown in Figs 10–13 for some values of Ca . The curtain profiles (Fig. 10) clearly demonstrate the trend routinely observed in experiments: as the substrate velocity increases, the contact angle also increases, and, as a consequence, the contact line moves downstream.

Since in the model the contact angle is ‘negotiated’ by the surface densities at the contact line through the modified Young equation (15), the origin of the velocity dependence of the contact angle can be also illustrated by the calculated profiles of the surface density distributions along the interfaces. As one can see in Figs 11–13, variations in the substrate velocity lead to almost no variations in the surface density on the free surface, which remains close to its equilibrium value $\bar{\rho}_{1e}^s$, whereas on the solid substrate the surface density varies strongly from the equilibrium value $\bar{\rho}_{2e}^s$ far downstream to a much smaller value at the contact line. As U increases, the latter gets closer to the surface density value on the free surface. Thus, the contact angle appears to be controlled by the surface density in the liquid–solid interface and increases as U becomes larger.

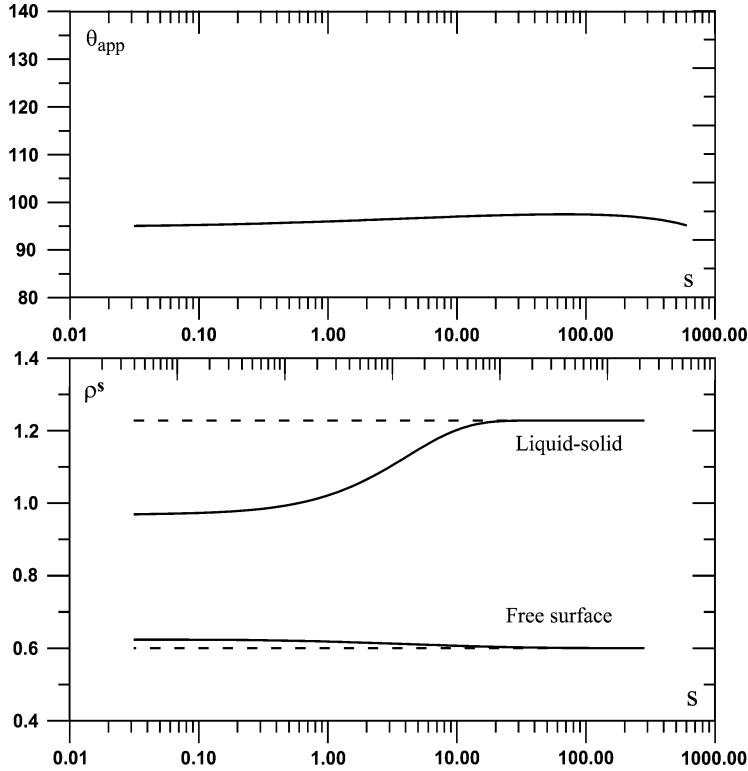


FIG. 12. Apparent contact angle θ_{app} and the distribution of the surface density ρ^s in curtain coating for $\text{Ca} = 0.02$. The equilibrium values of the surface density are shown by the dashed line.

It is important to note that, as one can see in Figs 11–13, the actual relaxation of the surface variables to their equilibrium values takes place over a length scale which is much larger than the ‘nominal’ relaxation length $U\tau$. If we formally define the actual ‘length of exponential relaxation’ along the liquid–solid interface s_r^n by

$$\rho^s(s_r^n) = \bar{\rho}_{2e}^s - (\bar{\rho}_{2e}^s - \rho_2^s(0))/e$$

(e is the base of the natural logarithm), then, as one can see in Table 1, s_r^n varies approximately from $2U\tau$ to $30U\tau$ as Ca decreases from 0.04 to 0.0025. It is also interesting to note that the values of s_r^n obtained in this formal way are very close to the asymptotic values l_r calculated by means of (71). Remarkably, despite strong variations in the distributions of the surface parameters along the solid surface on the scale $s < 3s_r^n$, there is little variation in the free surface profile on the same scale. This is illustrated by the plots of the apparent angle θ_{app} (see Fig. 1 for the definition) on the distance from the contact line shown in Figs 11–13 for different capillary numbers.

Finally, consider the performance of the matching of the BIE and FE solutions that the combined method uses at the ‘internal interface’ Γ_{ab} . This can be illustrated by the picture of the streamlines as they cross this ‘interface’. In Fig. 14, the arrows outside the frame show where Γ_{ab} intersects with it, but an inspection of the plots of the streamlines does not allow one to note where the contour Γ_{ab} actually lies within the picture. In other words, the internal interface has no effect on the flow. This has, of course,

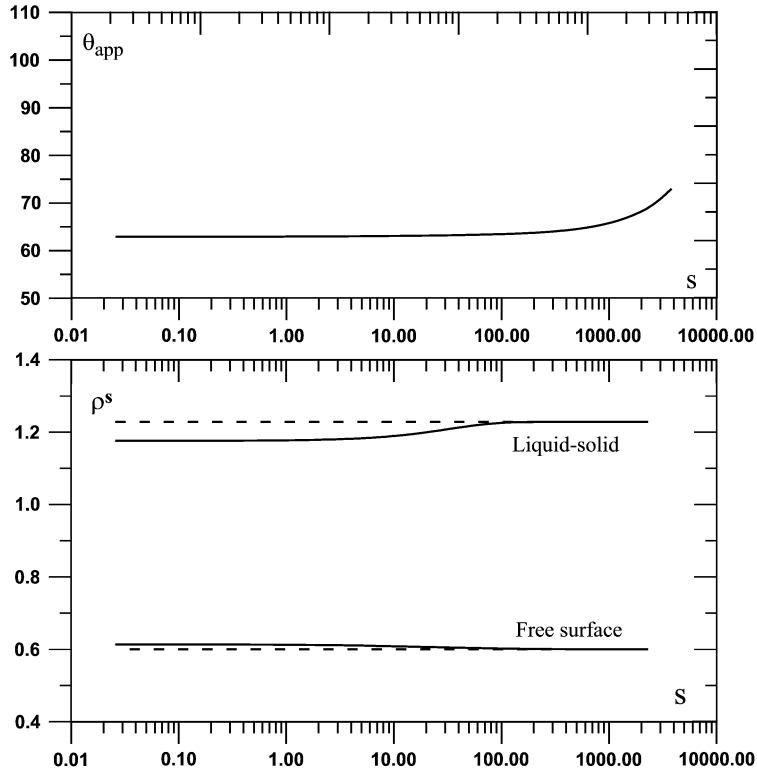


FIG. 13. Apparent contact angle θ_{app} and the distribution of the surface density ρ^s in curtain coating for $\text{Ca} = 0.0025$. The equilibrium values of the surface density are shown by the dashed line.

TABLE 1 A comparison of the actual relaxation length calculated numerically s_r^n with the asymptotic value $l_r = k_\rho^{-1}$ calculated by means of (71). Both s_r^n and l_r are scaled with $U\tau$

Ca	0.04	0.03	0.02	0.01	0.005	0.0025
s_r^n	2.3	2.9	4.3	8.8	16.7	33.1
l_r	2.5	3.2	4.5	8.4	16.3	32.2

been checked quantitatively. In the whole range of parameters, it has also been routinely checked that the simulation results are not sensitive, within the accuracy of the computations, to the position of Γ_{ab} , which was varied between 30 and $150l_r$.

A feature of the flow field worth noting is that, as a magnified view of the stream lines in the close vicinity of the contact line shows (Fig. 15), the streamlines go into the liquid–solid interface. This follows from ρ^s being significantly below its equilibrium value $\bar{\rho}_{2e}^s$ along the relaxation zone and hence, according to (26), one has adsorption of the fluid by the liquid–solid interface. The plots of ρ^s on the free surface indicate that there is desorption from the liquid–gas interface ($\rho^s > \bar{\rho}_{1e}^s$ there) so that in the immediate vicinity of the contact line, one has a uniform flow from the free surface into the liquid–solid interface. This type of flow is described qualitatively in Shikhmurzaev (2006). What is important to note

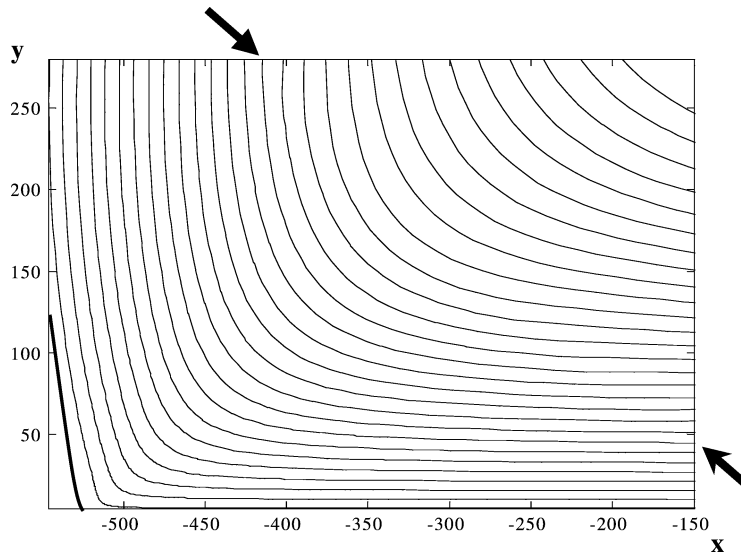


FIG. 14. Typical pattern of streamlines with the distances measured in nominal relaxation lengths $U\tau$. The points where the numerical ‘internal interface’ Γ_{ab} intersects the frame are indicated by the arrows; $Ca = 0.02$.

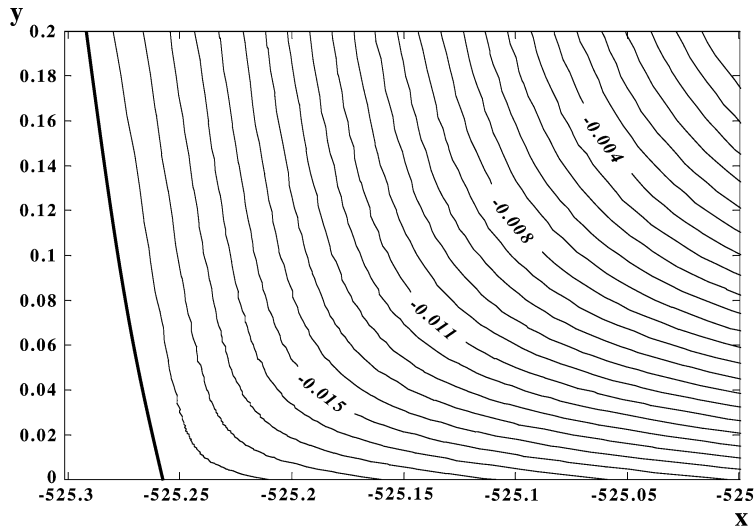


FIG. 15. A magnified view of the flow near the contact line showing adsorption of the fluid by the liquid–solid interface; $Ca = 0.02$.

for numerical calculations of dynamic wetting is that the interface disappearance/formation process leads to the interfaces no longer being streamlines, even for steady flows. This should be taken into account in adapting standard packages to incorporate the interface formation model since in many such packages, the ‘impermeability’ of interfaces is built in on a very deep level.

6. Conclusions

The developed method allows one to solve a variety of free boundary problems for the Stokes equations, including problems arising in the area of dynamic wetting, in an efficient way, with the finite-element component providing the accuracy and high spatial resolution in the key regions and the boundary integral equation component ensuring overall efficiency in describing the flow parameters in the main part of the flow domain. The matching of the two elements is straightforward, and it can be used to optimize the algorithm. The calculations of free boundary problems in the framework of the interface formation model, where the dynamic contact angle is part of the solution and hence the bulk, surface and contact line parameters become interrelated, require special attention to the accuracy and the spatial resolution within the relaxation zone which can stretch far beyond the ‘nominal’ relaxation length $U\tau$, especially when this length is small. The existing asymptotic solution provides an accurate estimate for the size of the relaxation zone.

REFERENCES

- BALLANDRAS, S., REINHARDT, A., LAUDE, V., SOUFYANE, A., CAMOU, S., DANIAU, W., PASTUREAUD, T., STEICHEN, W., LARDAT, R., SOLAL, M. & VENTURA, P. (2004) Simulations of surface acoustic wave devices built on stratified media using a mixed finite element/boundary integral formulation. *J. Appl. Phys.*, **96**, 7731–7741.
- BLAKE, T. D., BRACKE, M. & SHIKHMURZAEV, Y. D. (1999) Experimental evidence of nonlocal hydrodynamic influence on the dynamic contact angle. *Phys. Fluids*, **11**, 1995–2007.
- BLAKE, T. D. & SHIKHMURZAEV, Y. D. (2002) Dynamic wetting by liquids of different viscosity. *J. Colloid Interface Sci.*, **253**, 196–202.
- GASKELL, P. H., THOMPSON, H. M. & SAVAGE, M. D. (1999) A finite element analysis of steady viscous flow in triangular cavities. *Proc. Inst. Mech. Eng.*, **213C**, 263–276.
- GRESHO, P. M. & SANI, R. L. (2000) *Incompressible Flow and the Finite Element Method*. New York: Wiley.
- JASWON, M. A., MAITI, M. & SYMM, G. T. (1967) Numerical biharmonic analysis and some applications. *Int. J. Solids Struct.*, **3**, 309–332.
- JASWON, M. A. & SYMM, G. T. (1977) *Integral Equation Methods in Potential Theory and Elastostatics*. London: Academic Press.
- KELMANSON, M. A. (1983a) Boundary integral equation solution of viscous flows with free surfaces. *J. Eng. Math.*, **17**, 329–343.
- KELMANSON, M. A. (1983b) An integral equation method for the solution of singular slow flow problems. *J. Comput. Phys.*, **51**, 139–158.
- KELMANSON, M. A. (2004) Hypersingular boundary integrals in cusped two-dimensional free-surface Stokes flow. *J. Fluid Mech.*, **514**, 313–325.
- KISTLER, S. F. & SCHWEIZER, P. M. (eds) (1997) *Liquid Film Coating*. London: Chapman & Hall.
- LI, G. & ALURU, N. R. (2004) Hybrid techniques for electrostatic analysis of nanoelectromechanical systems. *J. Appl. Phys.*, **96**, 2221–2231.
- LUKYANOV, A. & SHIKHMURZAEV, Y. D. (2006) Curtain coating in microfluidics and the phenomenon of nonlocality in dynamic wetting. *Phys. Lett. A*, **358**, 426–430.
- MARQUEZ, A., MEDDAHI, S. & SELGAS, V. (2004) A new BEM-FEM coupling strategy for two-dimensional fluid-solid interaction problems. *J. Comput. Phys.*, **199**, 205–220.
- MOFFATT, H. K. (1964) Viscous and resistive eddies near a sharp corner. *J. Fluid Mech.*, **18**, 1–18.
- PEETERS, M. F., HABASHI, W. G. & DUECK, E. G. (1987) Finite-element stream function-vorticity solutions of the incompressible Navier-Stokes equations. *Int. J. Numer. Methods Fluids*, **7**, 17–27.

- POZRIKIDIS, C. (1992) *Boundary Integral and Singularity Methods for Linearized Viscous Flow*. Cambridge: Cambridge University Press.
- RALLISON, J. M. & ACRIVOS, A. (1978) A numerical study of the deformation and burst of a viscous drop in an extensional flow. *J. Fluid Mech.*, **89**, 191–200.
- SHIKHMURZAEV, Y. D. (1993) The moving contact line on a smooth solid surface. *Int. J. Multiphase Flow*, **19**, 589–610.
- SHIKHMURZAEV, Y. D. (1994) Mathematical modeling of wetting hydrodynamics. *Fluid Dyn. Res.*, **13**, 45–64.
- SHIKHMURZAEV, Y. D. (1997) Spreading of drops on solid surfaces in a quasi-static regime. *Phys. Fluids*, **9**, 266–275.
- SHIKHMURZAEV, Y. D. (2006) Singularities at the moving contact line. Mathematical, physical and computational aspects. *Physica D*, **217**, 121–133.
- SHIKHMURZAEV, Y. D. (2007) *Capillary Flows with Forming Interfaces*. London: Taylor & Francis.
- SQUIRES, T. M. & QUAKE, S. R. (2005) Microfluidics: fluid physics at the nanoliter scale. *Rev. Mod. Phys.*, **77**, 977–1026.
- TSAI, W.-T. & YUE, D. K. P. (1996) Computation of nonlinear free-surface flows. *Annu. Rev.*, **28**, 249–278.
- WILSON, M. C. T., SUMMERS, J. L., SHIKHMURZAEV, Y. D., CLARKE, A. & BLAKE, T. D. (2006) Nonlocal hydrodynamic influence on the dynamic contact angle: slip models versus experiment. *Phys. Rev. E*, **73**, 041606.
- ZINCHENKO, A. Z. & DAVIS, R. H. (2002) Shear flow of highly concentrated emulsions of deformable drops by numerical simulations. *J. Fluid Mech.*, **455**, 21–62.
- ZINCHENKO, A. Z., ROTHER, M. A. & DAVIS, R. H. (1999) Cusping, capture, and breakup of interacting drops by a curvatureless boundary-integral algorithm. *J. Fluid Mech.*, **391**, 249–292.